nature geoscience

SUPPLEMENTARY INFORMATION

DOI: 10.1038/NGEO977

Supplemental material to accompany *Complex rupture during the 12 January 2010 Haiti Earthquake*

G.P. Hayes[1], R.W. Briggs[1], A. Sladen[2], E.J. Fielding[3], C. Prentice[4], K. Hudnut[5,] P. Mann[6], F.W. Taylor[6], A.J. Crone[1], R. Gold[1], T. Ito[2,7], M. Simons[2]

This supplement describes the data collection and processing techniques for each individual component of our multi-disciplinary analysis of the rupture process of the 12 January 2010 Haiti earthquake (hereafter termed the 2010 Leogane earthquake). First we describe details of the finite fault modeling technique, and results for single-plane fault models using teleseismic data. Next we discuss InSAR data sources and detailed processing, before presenting details of the geological field deployment and data collection. Finally we present alternate joint inversions to our preferred kinematic rupture model (**figure 3**), comparing these models to the preferred solution, and discussing the relative merits of each. We present two alternate rupture models; a three-plane model (**figure S5**) to show the effects of north vs. south dip for fault B, the Leogane fault; and a three-plane model exploring the effects of initiating rupture on fault B rather than fault A, the EPGF-like structure (**figures S6-7**).

1. Teleseismic Bodywave Finite fault modeling

We invert for the rupture process of the earthquake using broadband teleseismic P- and SH- body waveforms recorded at GSN stations worldwide. Data were selected based upon quality (high signal-to-noise ratios) and azimuthal distribution. Waveforms are first converted to displacement by removing the instrument response and then used to constrain the slip history based on the finite fault inversion algorithm of Ji et al.[1]. To improve our resolution of rupture onset,

1. U.S. Geological Survey, Golden, CO
2. California Institute of Technology, Pasadena, CA
3. Jet Propulsion Laboratory, California Institute of Technology, Pasadena, CA
4. . U.S. Geological Survey, Menlo Park, CA
5. . U.S. Geological Survey, Pasadena, CA
6. University of Texas Institute of Geophysics, Jackson School of Geosciences, University of Texas, Austin
7. Nagoya University, Japan

DOI: 10.1038/NGEO977

directivity effects and the high-frequency aspects of the rupture history, we invert velocity body waveforms in addition to displacement records. We adopt the source parameters of the gCMT solution for our analyses, modifying the strike of the ϕ=251° fault plane such that it is consistent with the strike of the geomorphic expression of the Enriquillo Plantain Garden fault (EPGF) at the surface (**figure 1)**, approximately 264°. We constrain the rupture to propagate predominantly westward from the hypocenter of the earthquake, favored by the majority of aftershocks locating to the west of the mainshock (**figure 1**). Such directivity is also suggested by the variation in velocity records with azimuth (**figure S1**). Furthermore, we bury the top of the modeled fault plane by 1km and constrain the top cells of the model to slip no more than 1m, to produce a model that can match geological observations of no surface fault rupture along the EPGF (**supplementary material Section 3**). Adding these extra constraints to the inversion process does not significantly affect the fit of the model to the input data. We note that our inversion approach[1] is limited to the use of planar faults, rather than non-planar structures; while efforts to model rupture on non-planar structures have been proposed[2], these still require knowledge of fault geometry *a priori*, which is not available (nor known) in the case of this earthquake.

Results of this initial teleseismic-data-only finite fault model are shown in **figure S1**. Inversion results demonstrate peak slip of ~6.0 m updip and close to the hypocenter. Significant slip extends ~ 25-30 km west of the hypocenter, with a notable transition towards thrust motion with distance along strike and updip.

2. InSAR analysis

Synthetic aperture radar (SAR) interferometry analysis presented here used data acquired by the Japanese Aerospace Exploration Agency (JAXA) Advanced Land Observation Satellite (ALOS), with its phased-array L-band SAR instrument (PALSAR) that has a radar wavelength of 23.5 cm. The data was processed from the PALSAR Level 1.0 raw data with the JPL/Caltech ROI_pac SAR interferometry

package[3]. All scenes were acquired in the fine-beam single-polarization (FBS) mode. The topographic data used to calculate and remove the topographic phase was the Shuttle Radar Topography Mission (SRTM) 1-arcsecond posting digital elevation model with the data voids filled by the ASTER GDEM (R.E. Crippen, pers. comm.). Interferograms were analyzed with averaging (looks) of 8 samples across-track and 16 samples along-track, and were unwrapped with SNAPHU[4].

ALOS PALSAR data were processed from four satellite paths, three ascending (satellite moving northward) paths and one descending (satellite moving southward) path as shown in Table S1. All the PALSAR data was acquired with the standard 34.3° look angle (at the satellite) that results in line-of-sight (LOS) angles relative to the vertical at the Earth's surface varying from 36° to 41° across the radar swath. The LOS unit vector from the ground at the center of the swath to the satellite on the ascending paths is (-0.6080, -0.1337, 0.7826) for east, north, and up components, while the descending path has an LOS unit vector of (0.6080, -0.1337, 0.7826). Because the LOS vectors on the ascending and descending paths have opposite signs but equal magnitudes for the east component, and because the LOS does not change much across the PALSAR swath, we can calculate an approximation of the eastward ground displacements by taking the difference between the descending and ascending path interferogram values at each point and dividing by 2*0.608 (**figure 2**). Similarly, we can sum the values of the ascending and descending interferograms and divide by sqrt(N^2+U^2) to calculate the ground displacements in a direction that is 83% up and 17% south (**figure 2**).

Interferograms were downsampled to about 1000 points each using a distribution of samples optimized for determining the slip on a fault similar to the main fault used in the slip inversions[5].

DOI: 10.1038/NGEO977

Table S1. ALOS PALSAR pairs used for interferograms.

ALOS path	Date1	Date2	Bperp.* (m)
A136	2009/09/12	2010/01/28	800–838
A137	2008/02/09	2010/02/14	-400–-480
A138	2009/02/28	2010/01/16	1040–1141
D447	2009/03/09	2010/01/25	859–777

* Perpendicular component of baseline at center of swath from top to bottom of interferogram.

3. Geologic observations of coastal deformation

Extensive coastal deformation accompanied the 2010 Leogane earthquake. Analysis of high-resolution imagery obtained immediately after the event revealed uplifted coral reefs, widened beach faces, and extensive shaking-related lateral spreading, compaction, and liquefaction along approx. 50 km of coastline extending from Gressier to Port Royal (**figure 2**). These observations were confirmed during field work from 25 February to 4 March 2010[6]. We collected detailed measurements of vertical deformation at 19 sites (**table S2**), and we supplement these measurements with qualitative observations of vertical displacements (**table S3 and figure S2**).

Coral methods

Coral microatolls are sensitive recorders of vertical fluctuations in sea level[7] and this makes them useful instruments for recording vertical tectonic deformation[8]. Colonies of *Siderastrea siderea* and *Diploria strigosa* form the most commonly encountered microatolls along the affected coast. Several other species that record clear pre-earthquake highest levels of survival (HLS) were also useful for assessing

2010 vertical displacement, including *Millepora complanata, Porites astreoides, Porites porites, Porites furcata, Diploria labyrinthiformis, Montastraea annularis,* and *Siderastrea radians.*

At sites where reefs record uplift we surveyed multiple microatoll and coral HLS elevations with respect to sea level. Ten or more measurements from each coral species were collected unless fewer heads were available. We also recorded the elevation difference between pre- and post-earthquake HLS; in every case we anticipate that this will underestimate the final diedown of the heads because the lowest tides between the time of the earthquake and our visit occurred mainly at night. Diedowns of the fire coral *Millepora* are frequently observed and offer minimum estimates of uplift (**table S2**) and qualitative evidence of reef displacement.

Because Haiti lacks permanent tide gauges, we establish a model tidal curve to provide tidal a datum for our survey measurements and calibrate this model to a temporary tide gauge deployment. Because of the small tidal range (70-80 cm) and relatively simple shape of the tidal curve in the region, we first generate a prediction for nearby Port-au-Prince using the program Xtide (http://www.flaterco.com/xtide/) to capture the general shape of the curve. We then shift the curve in phase to fit observations at Gonave island (Roger Bilham, personal comm.). Visual comparison of the model curve with the Gonave observations, and comparison with sea level measurements collected at each uplift site, are consistent with less than 5 cm of misfit, which we subsequently incorporate into the total uplift uncertainties.

We use a tectonically stable site at Ile de la Gonave to establish how microatoll HLS relates to annual extreme low tide (ELT) in this region. Gonave appears to have remained tectonically inactive for the last 125 ka[9], and a long period of tectonic stability at the Ile de la Gonave site has led to the formation of a bioerosion notch and overhang at water level that is several meters deep along most of the limestone coast. We did not observe any evidence of uplift at the site due to the 2010 Leogane

DOI: 10.1038/NGEO977

earthquake rupture. At the site *Siderastrea siderea*, *Diploria strigosa*, and *Porites astreoides* survive on average 6 cm, 8 cm, 2 cm above ELT, respectively. We utilize these corrections in our calculations of total uplift (**table S2**).

Sea surface height (SSH) anomalies complicate assessments of microatoll uplift because they impart a climatic signal to coral head growth that must be recognized and removed. A plot of sea surface anomalies at our study sites as measured by TOPEX/POSEIDON and Jason-1 (**figure S4**) shows that anomalies are typically ± 7 cm about mean sea level[10]. A large excursion in 2009/2010 of -15 cm is recorded on most Siderastrea microatolls as a fresh die-down of up to 8 cm prior to 12 January. Because the HLS created during this SSH excursion is not tectonic and does not represent the pre-earthquake elevation of the microatolls, we use the higher and older 2009 HLS to calculate tectonic uplift in 2010. Because the relationship between SSH anomalies and microatoll growth appears to be complex (that is, the SSH anomalies do not exactly equal observed diedowns), we assign a large uncertainty of ±10 cm to the SSH anomaly contribution to our uplift calculations.

At four sites corals are not available. At three of these (Kay Mirak, Kay Tiyout, and Tapion de Petit Anglais; **table S2**) we derive uplift estimates from beach geomorphic features. A storm during the night of 25 February caused a coarse storm berm to form along most of the surveyed coast, and we measured the difference between pre- and post-earthquake storm berms as a proxy for uplift. We face a different challenge at the pier in Petit Goave, where possible tectonic subsidence along the coast is masked by secondary sliding and slumping due to ground shaking. Here the concrete pier appears level and undeformed, and there is no significant secondary deformation along a transect extending 1 km inland. The 15 cm of subsidence we report at the Petit Goave pier is based on eyewitness accounts and the depth of standing water adjacent to the pier in a location that was not previously flooded but was inundated daily after 12 January. Because these are only crude indicators of uplift, we apply an arbitrary uncertainty of ±30% to these measurements.

Geologic observations of coseismic deformation

The relatively simple vertical deformation pattern indicates a bulge of uplift centered beneath the Leogane fan delta and the ocean floor to the west (**figure 2** and **figure S2**). Uplift is highest (0.64 ± 0.11 m) at Beloc and decreases to the north and south. At the easternmost surveyed site (Passion Beach near Gressier) uplift is only 0.07 ± 0.07 m, indicating that relatively little fault slip extended beneath and eastward of this point. Along the east-west trending coast between Bellevue and Petit Goave uplift is generally less than 0.40 m. Uplift decreases to 0.05 ± 0.05 m at the La Hatte seawall in Petit Goave, and then reverses in sign to subsidence at the Petit Goave pier. The hingeline between these two points appears to mark the western extent of the main rupture zone (**figure S2**). A small amount of uplift is observed at Port Royal island (0.09 ± 0.09 m), where the reef was unaffected at the time of our visit. Apparent subsidence of -0.21 ± 0.11 m adjacent to Port Royal Point appears to reflect displacement across the Port Royal fracture, an ambiguous feature that may represent coseismic normal displacement, motion during an aftershock, or triggered slip.

Comparison of the geologic and InSAR-derived measurements of tectonic uplift along the western margin of the Leogane fan delta are shown in **figure 2**. As discussed in the main manuscript, the results are in general agreement.

4. Alternative Kinematic Source Inversions

Here we present two alternative rupture models, contrasting our favoured solution (**figure 3**) with: (i) a model evoking slip on a 55° south-dipping plane rather than on a north-dipping blind thrust **(figure S5)**; and (iii), a model exploring the effects of initiating slip on the north-dipping Leogane fault rather than on the EPGF-like structure (**figures S6-7**).

In the first scenario (**figure S5**), the alternate model explains some but not all of the features of the data, with slightly poorer residuals than our preferred solution (an

DOI: 10.1038/NGEO977

increase in misfit of 15%). However, the model does not fit the broad subsidence trough in the InSAR data south of the EPGF, and does not fit the left-lateral motion identified by seismology, nor the patch of eastward motion to the northeast of the earthquake hypocenter (see main text for discussion of these features). This model, in fact, suggests almost entirely pure thrust motion on the Leogane fault (**figure S5c**), apart from a small left-lateral component of slip close to the surface in the bay, in violation of both seismological observations and campaign GPS vectors in the epicentral region[11]. The presence of pure thrust motions here is an indication that the model prefers right-lateral motions on this plane, which our inversion constraints (see *Methods* section, main manuscript) do not allow. This model also includes significant moment release later than observed in seismic inversions (**figure S1**), as a result of large amounts of slip offshore and to the west of the Leogane delta, where InSAR and geological observations have little constraint. Significant slip occurs here to satisfy matching the moment release of the earthquake in the inversion, and because InSAR and geological uplift data constrain well the lower amounts of slip on the (now shallow) fault in the delta region further east.

We motivate our second alternate model by performing Coulomb stress transfer calculations[12], which show favourable stress transfer conditions for rupture initiating on the Leogane fault and subsequently triggering slip on the EPGF-like structure (**figure S6c**), but unfavourable conditions for the reverse scenario (**figures S6a-b**). The rupture model for this inversion (**figure S7**) reproduce our observations well, marginally less than our favoured solution (an increase in misfit of 3%), but cannot explain the first motions observed for the event (**figure S12**), which indicate dilatational motions to the north and northwest of the epicenter in a region of the focal sphere where this model requires compressional motion. Because of this major misfit, we prefer a solution in which the earthquake nucleates on the EPGF-like structure, dynamically triggering slip approximately 10 km to the north on the Leogane fault after a small time delay (**figure 3**), though we note the ambiguity in these solutions due to the compact and complex nature of this rupture.

References

1. Ji, C., Wald, D.J. & Helmberger, D.V. Source description of the 1999 Hector Mine, California, earthquake, part I: Wavelet domain inversion theory and resolution analysis. *Bull. Seis. Soc. Amer.* **92**, 1192-1207 (2002).

2. Wald, D., Ji, C., and Hayes, G.P., 2008. Global earthquake characterization on irregular fault surfaces, *Eos Trans. AGU* **89(53)**, Fall Meet. Suppl., Abstract S31C-01.

3. Rosen, P.A., Hensley, S., Peltzer, G., & Simons, M. Updated repeat orbit interferometry package released: Eos Trans. Amer. Geophys. Union **85**, 47 (2004).

4. Chen, C.W., & Zebker, H.A. Phase unwrapping for large SAR interferograms: statistical segmentation and generalized network models. *IEEE Trans. Geosc. Remote Sensing* **40**, 1709-1719 (2002).

5. Lohman, R.B., & Simons, M. Some thoughts on the use of InSAR data to constrain models of surface deformation: Noise structure and data downsampling. *Geochem. Geophys. Geosyst*. **6**, doi:10.1029/2004GC000841 (2005).

6. Prentice, C.S., et al. Seismic hazard of the Enriquillo-Plantain Garden Fault in Haiti inferred from paleoseismology. *Nature Geosci.*, doi:10.1038/ngeo991 (in press).

7. Scoffin, T.P., Stoddart, D.R. & Rosen, B.R. The nature and significance of microatolls. *Philos. Trans. R. Soc. London Ser. B* **284**, 99-122 (1978).

8. Taylor, F.W., Frohlich, C., Lecolle, J. & Strecker, M. Analysis of partially emerged coals and reef terraces in the central Vanuatu arc: comparison of contemporary coseismic and nonseismic with Quaternary vertical movements. *J. Geophys. Res.* **92**, 4905-4933 (1987).

9. Mann, P., Taylor, F.W., Edwards, R.L. & Ku, T-L. Actively evolving microplate formation by oblique collision and sideways motion along strike-slip faults: An example from the northeastern Caribbean plate margin. *Tectonophys.* **246**, 1-69 (1995).

10. Leuliette, E. W, R. S. Nerem, and G. T. Mitchum. Calibration of TOPEX/Poseidon and Jason altimeter data to construct a continuous record of mean sea level change. *Marine Geodesy*, **27**(1-2), 79-94 (2004).

11. Calais, E., et al. Transpressional rupture of an unmapped fault during the 2010 Haiti earthquake. *Nature Geosci.,* doi:10.1038/ngeo992 (in press).

12. Lin, J. and R.S. Stein. Stress triggering in thrust and subduction earthquakes, and stress interaction between the southern San Andreas and nearby thrust and strike-slip faults, *J. Geophys. Res.,* **109**, doi:10.1029/2003JB002607 (2004).

DOI: 10.1038/NGEO977

Figure Captions

Figure S1: 2010 Leogane Earthquake Teleseismic Rupture Model. (a) Preferred single-plane source inversion using teleseismic body-wave data. Fault modeled using an adjusted plane from the gCMT moment tensor solution, with strike, ϕ=264° and dip, ∂=70°, unilateral rupture on a plane buried to a depth of 1 km, and tapered slip in the shallowest subfaults. Color represents subfault slip magnitude; black arrows represent slip direction. Contours represent the position of the rupture front with time, plotted at 5s intervals. The rate of moment release with time is shown in **(b)**. Waveform fits are shown in **(c)**, both for P- and SH-wave displacement (top) and velocity (bottom) records. Relative weights are represented by thickness of data (black) and synthetics (red). Dashed records have zero weight. Numbers at the beginning of each record represent distance (bottom) and azimuth (top) to station, while numbers at the end of each record represent the peak amplitude of the data.

Figure S2. Qualitative observations of coastal uplift. Zones of uplift, subsidence, secondary (shaking-related) subsidence, or no apparent change are denoted. Site numbers are from **Table S3**. A transition from uplift to stability and apparent tectonic subsidence occurs at Petit Goave. The observations are not exhaustive but are intended to complement the quantitative measurements of uplift presented in **Figure 2** and **Table S2**.

Figure S3. Multiple dissolution notches on limestone rockfall block adjacent to the Tapion Ridge. Indicated by arrows; the upper notch may represent sea level prior to uplift during previous 2010-type events.

Figure S4. Sea-surface height (SSH) anomalies. Anomalies from 1993-2010 in the study area[10], derived from TOPEX/POSEIDON and Jason-1 altimetry data.

Figure S5. Alternative kinematic rupture model 1. From the joint inversion of all data, using a 45° south dipping fault plane in place of the north-dipping (Leogane) fault most dominant in the earthquake rupture of our preferred solution. Panel (a) shows the modeled slip distribution, contoured in 50 cm increments. Thick coloured lines (red, blue, purple) represent the top of each fault (A, B, C, respectively). Numbered blue squares represent major population centers: 1= Port au Prince, 2 = Leogane, 3 = Port Royal. Panel (b) shows the rupture model in plan view; arrows represent the slip direction on each subfault, scaled by slip amplitude. The 6s rupture contour (dashed lines) is labelled for reference. (c) Shows the moment tensor solution (top) and moment rate function (bottom) for this solution.

Figure S6. Coulomb stress transfer between primary faults. Models of static stress transfer to investigate the most likely rupture order for fault A, the steep lateral EPGF-type structure, and fault B, the blind thrust structure (Leogane fault). **(a)** and **(b)** show the Coulomb stress change imposed by 1.0m of left-lateral slip on the eastern half of the EPGF-type fault, onto thrust faults oriented 257°/55°/90° (the eastern half of slip on the Leogane fault). **(c)** and **(d)** show the Coulomb stress change imposed by 1.0m of left-lateral slip on the eastern half of the EPGF-type fault, onto thrust faults oriented 257°/55°/45° (the western half of slip on the Leogane fault). **(e)** and **(f)** show the Coulomb stress change imposed by 2.0m of reverse slip on the eastern half of the Leogane fault, onto left-lateral strike slip faults oriented 83°/70°/0° (the eastern half of slip on the EPGF-type fault). Faults are outlined in black; surface fault expressions are shown by green lines. In **(e)**, slip on the Leogane fault is tapered towards the surface from 2.0-0.0 m from 5-0 km along the dip-direction of the fault. Blue dashed lines in **(b), (d)** and **(f)** show the calculation depths in **(a), (c)** and **(e)**.

DOI: 10.1038/NGEO977

Figure S7. Alternative kinematic rupture model 2. From the joint inversion of all data, nucleating rupture on the north-dipping (Leogane) fault. Panel (a) shows the modeled slip distribution, contoured in 50 cm increments. Thick coloured lines (red, blue, purple) represent the top of each fault (A, B, C, respectively). Numbered blue squares represent major population centers: 1= Port au Prince, 2 = Leogane, 3 = Port Royal. Panel (b) shows the rupture model in plan view; arrows represent the slip direction on each subfault, scaled by slip amplitude. The 6s rupture contour (dashed lines) is labelled for reference. The view of fault B, the Leogane fault, is through the plane (i.e. viewed from below the north dipping plane). (c) Shows the moment tensor solution (top) and moment rate function (bottom) for this solution.

Figure S8. Teleseismic waveform fits for proposed kinematic rupture model. Data (black) and synthetic (red) seismograms are aligned on the P or SH arrivals. The number at the end of each trace is the peak amplitude of the data. The number above the beginning of each trace is the source azimuth and below is the epicentral distance. In the inversion process, P-waves are weighted 2x SH-waves.

Figure S9. InSAR data fits for proposed kinematic rupture model. Model fits are shown for each of the 4 unwrapped ascending and descending (top), and wrapped descending (bottom) ALOS PALSAR interferograms. The first and second columns show the data and model. The third column describes the residual between the model and data. “Ramp” describes the correction applied to the InSAR images to account for uncertainties in the signal, such as orbital errors.

Figure S10. Coastal uplift observation fits for proposed rupture model. Observations (black), compared to predictions (red) from our proposed model, overlain on surface projection of the coseismic slip distribution.

Figure S11. Assessment of Leogane earthquake W-Phase CMT solution sensitivity to fault plane dip. **(a)** Mechanisms constrained to a pure double-couple. RMS plotted relative to best-fitting non double-couple solution (star). Blue = relative RMS measure, red = absolute. In **(b)**, we show the CMT solutions for our best-fitting rupture model, gCMT, the USGS W-Phase inversion, and the USGS first motion double-couple solution.

Figure S12. First motion focal mechanism of the Leogane earthquake. Best fit to teleseismic P-wave first-motions, courtesy of George Choy, USGS NEIC, and the NEIC Preliminary Determination of Epicenters Bulletin (http://earthquake.usgs.gov/research/data/pde.php). Blue circles represent dilatational (negative) first motions, red triangles compressional (positive), and white squares nodal observations. Gray shading represents the compressional quadrants of the best double-couple solution. Dotted line represents the best double-couple of the gCMT moment tensor solution. “P” and “T” represent the P- and T-axes of each solution.

DOI: 10.1038/NGEO977

Figure S1

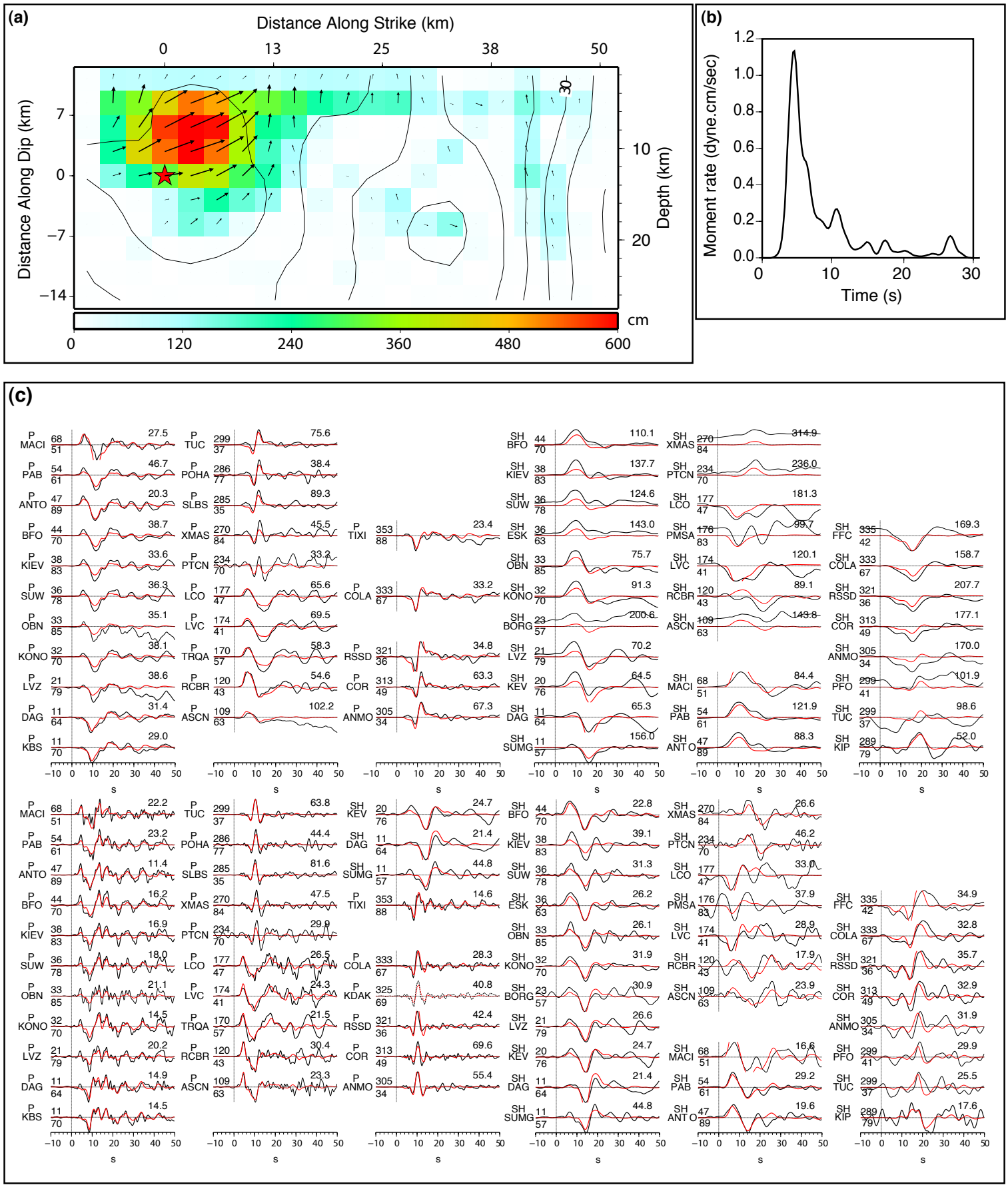

Figure S2

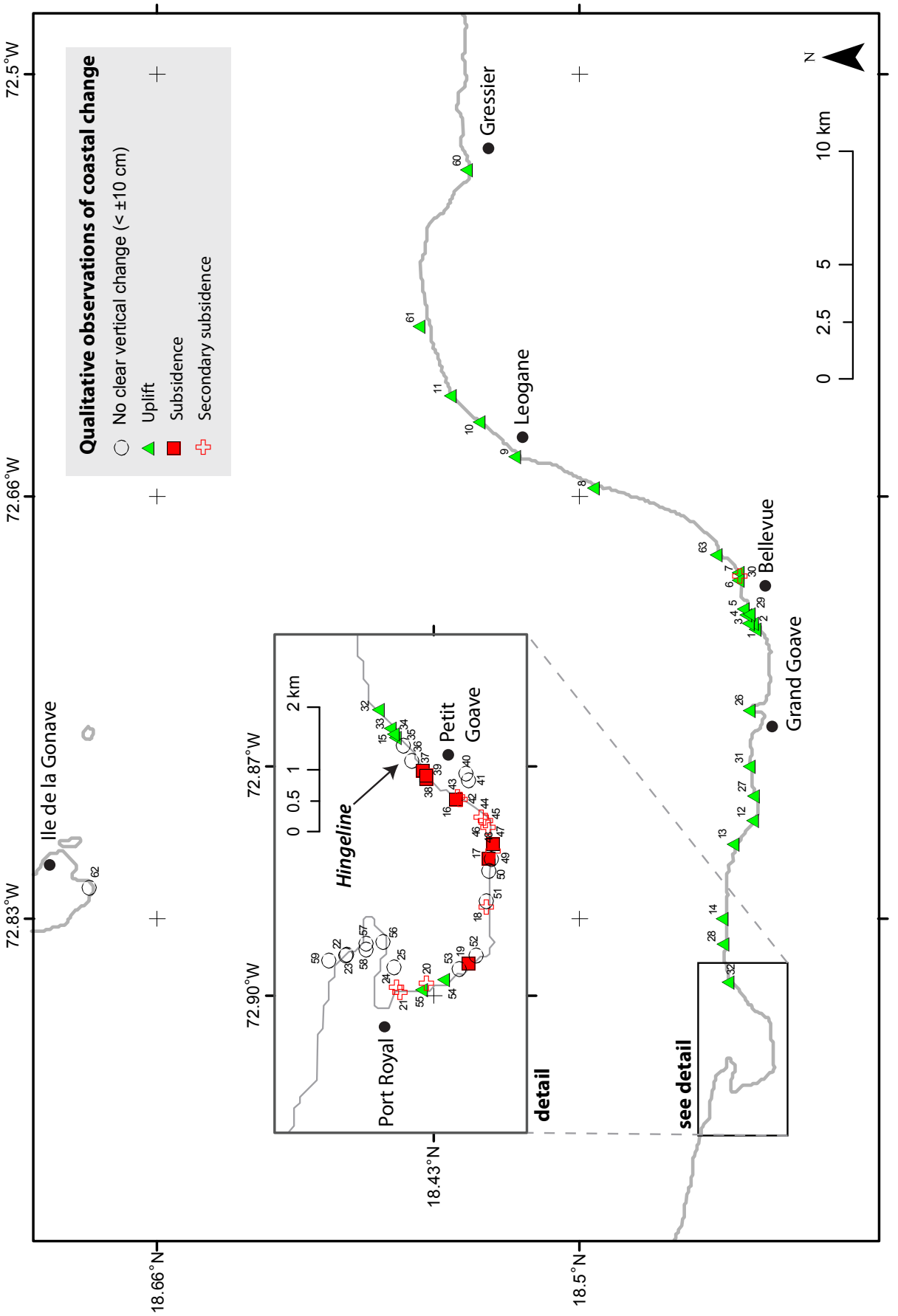
Qualitative observations of coastal change
No clear vertical change (< ±10 cm)
Uplift
Subsidence
Secondary subsidence
72.5°W
72.66°W
72.83°W
18.66°N
18.5°N
18.43°N
72.87°W
72.90°W
Ile de la Gonave
Gressier
Leogane
Bellevue
Grand Goave
Petit Goave
Port Royal
Hingeline
detail
see detail
N
0 2.5 5 10 km
0 0.5 1 2 km

DOI: 10.1038/NGEO977

Figure S3

Figure S4

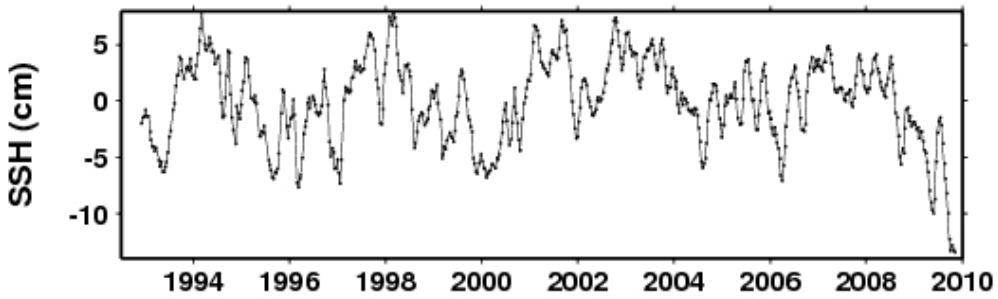

DOI: 10.1038/NGEO977

Figure S5

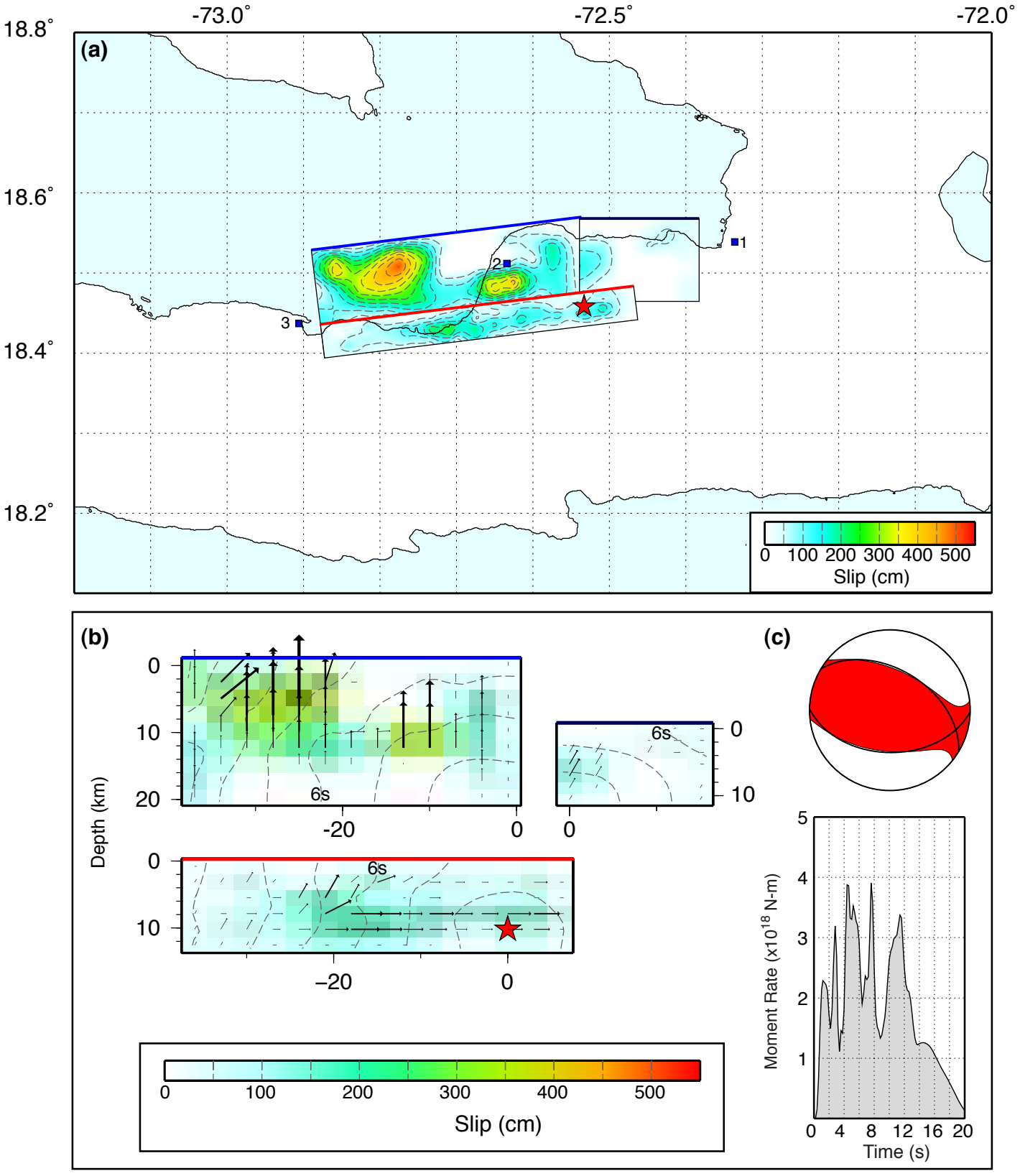

Figure S6

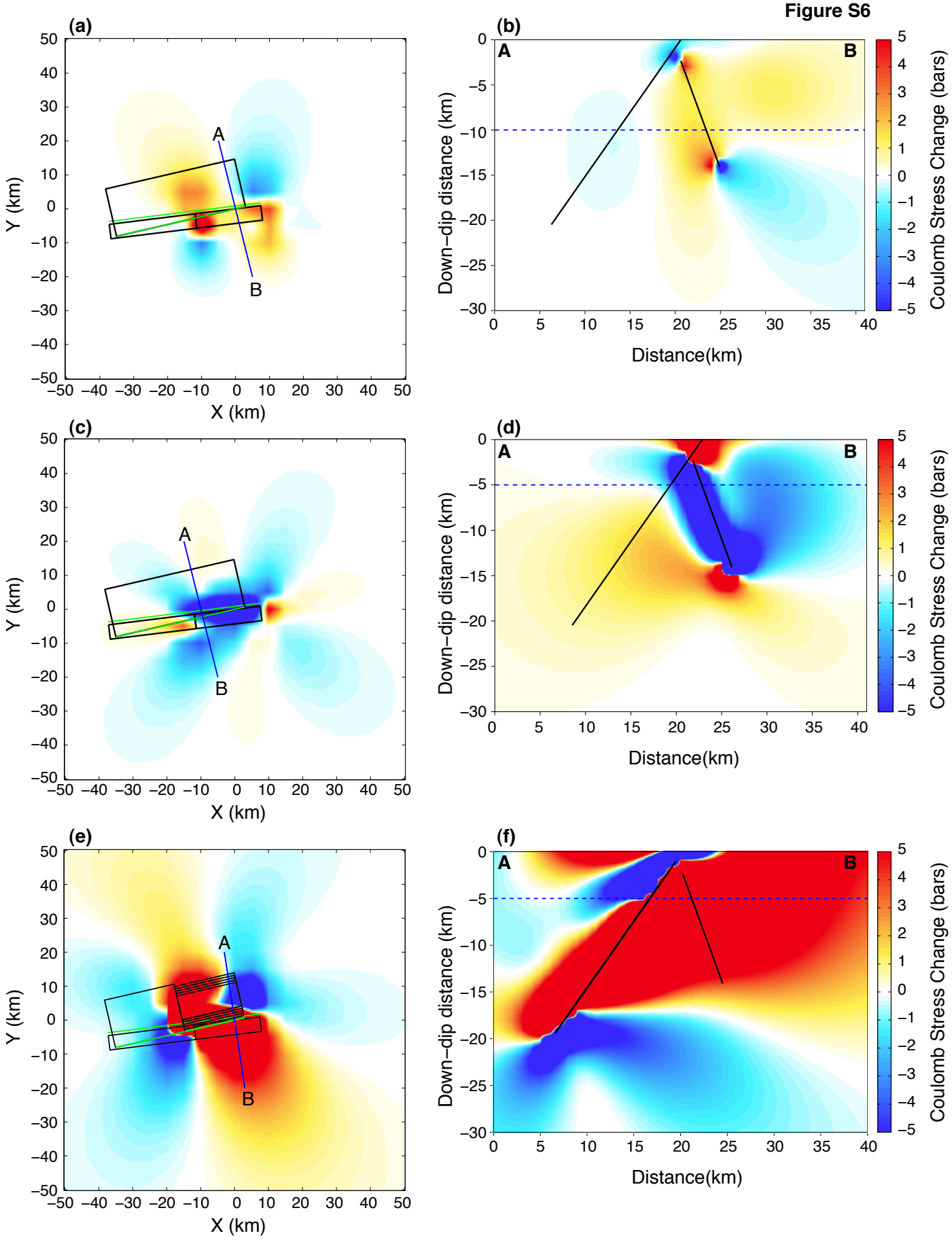
(a)
(b)
(c)
(d)
(e)
(f)
A
B
Y (km)
X (km)
Down−dip distance (km)
Distance(km)
Coulomb Stress Change (bars)

DOI: 10.1038/NGEO977

Figure S7

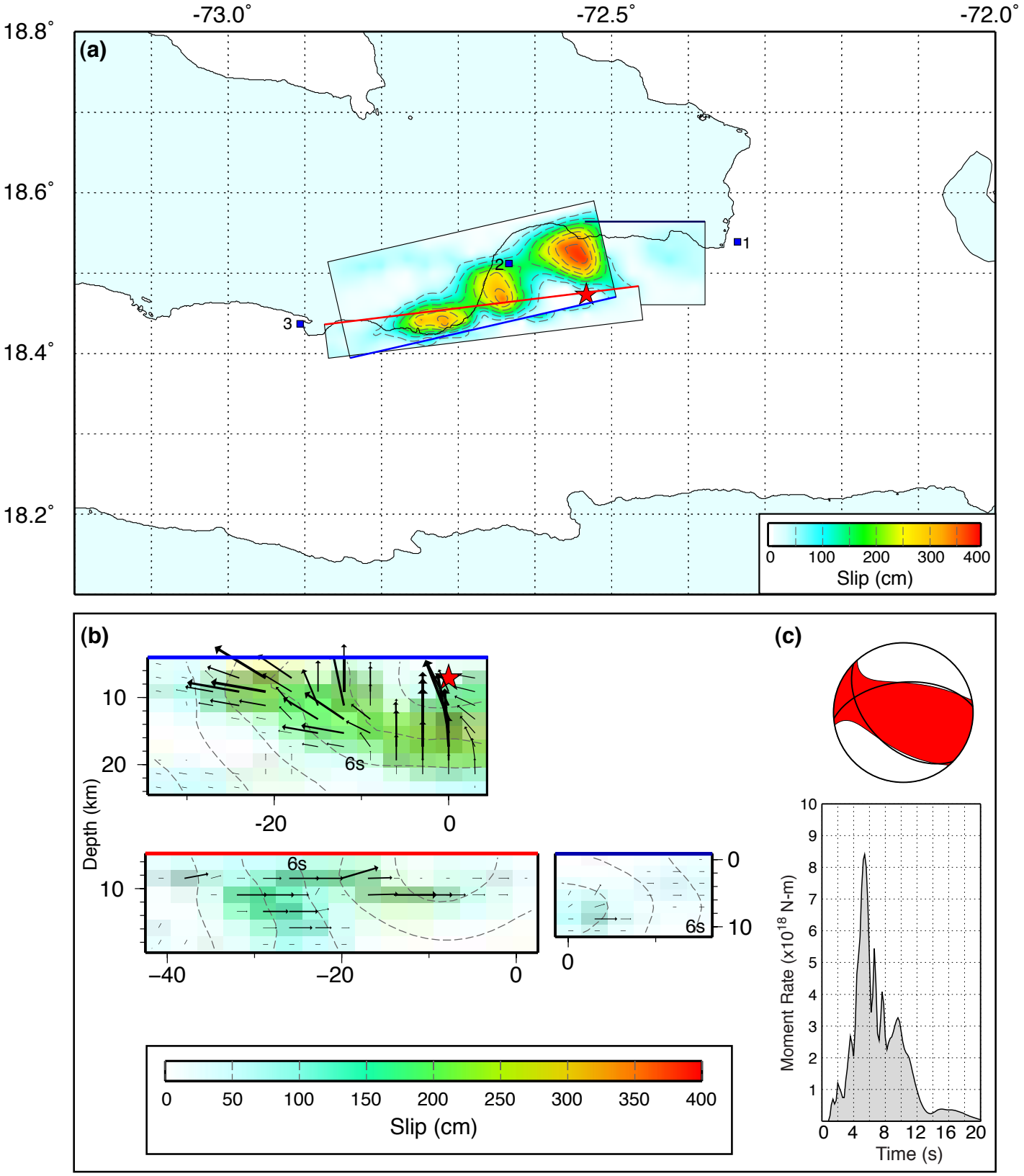

Figure S8

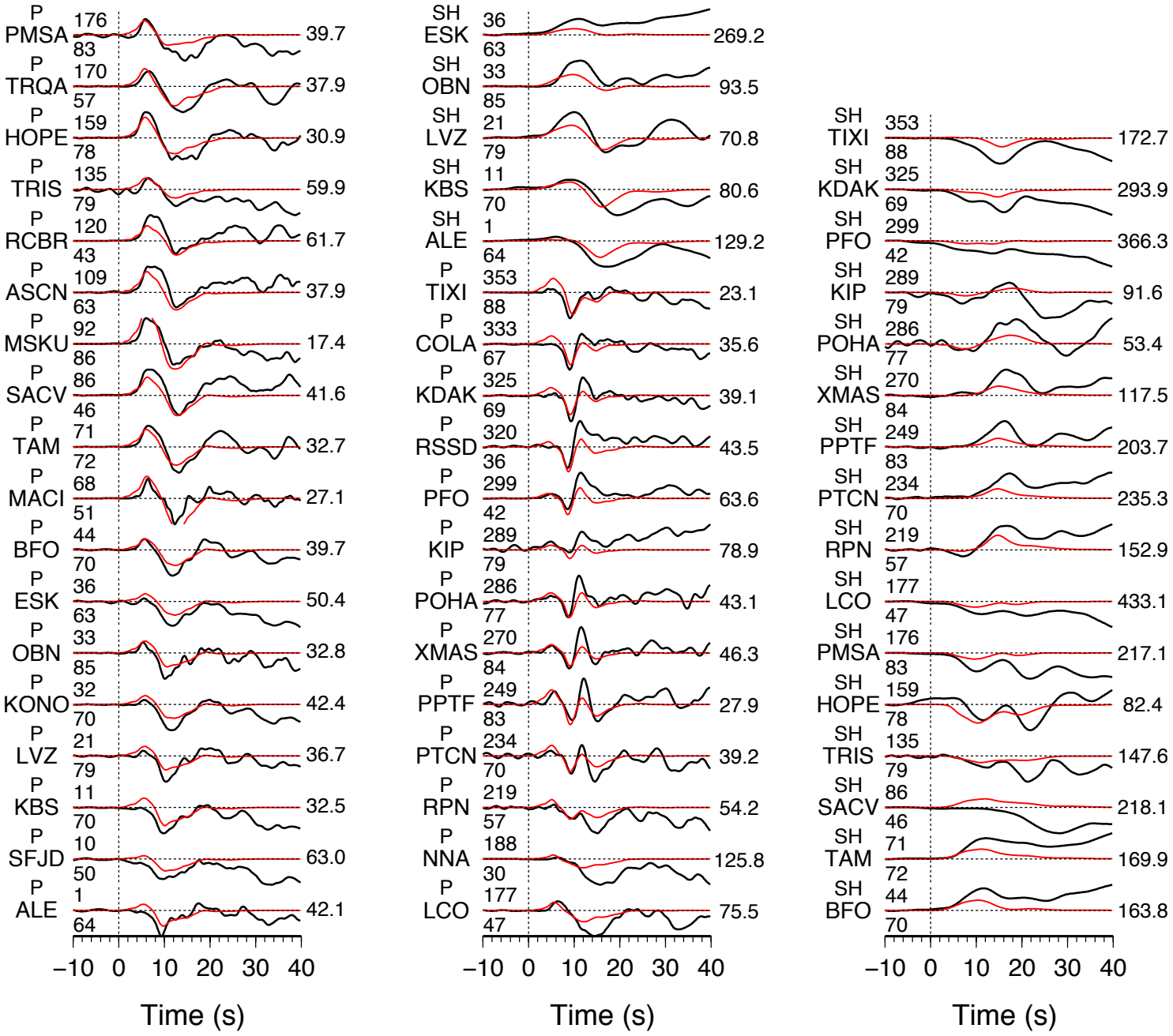
P PMSA 176 83 39.7
P TRQA 170 57 37.9
P HOPE 159 78 30.9
P TRIS 135 79 59.9
P RCBR 120 43 61.7
P ASCN 109 63 37.9
P MSKU 92 86 17.4
P SACV 86 46 41.6
P TAM 71 72 32.7
P MACI 68 51 27.1
P BFO 44 70 39.7
P ESK 36 63 50.4
P OBN 33 85 32.8
P KONO 32 70 42.4
P LVZ 21 79 36.7
P KBS 11 70 32.5
P SFJD 10 50 63.0
P ALE 1 64 42.1
SH ESK 36 63 269.2
SH OBN 33 85 93.5
SH LVZ 21 79 70.8
SH KBS 11 70 80.6
SH ALE 1 64 129.2
P TIXI 353 88 23.1
P COLA 333 67 35.6
P KDAK 325 69 39.1
P RSSD 320 36 43.5
P PFO 299 42 63.6
P KIP 289 79 78.9
P POHA 286 77 43.1
P XMAS 270 84 46.3
P PPTF 249 83 27.9
P PTCN 234 70 39.2
P RPN 219 57 54.2
P NNA 188 30 125.8
P LCO 177 47 75.5
SH TIXI 353 88 172.7
SH KDAK 325 69 293.9
SH PFO 299 42 366.3
SH KIP 289 79 91.6
SH POHA 286 77 53.4
SH XMAS 270 84 117.5
SH PPTF 249 83 203.7
SH PTCN 234 70 235.3
SH RPN 219 57 152.9
SH LCO 177 47 433.1
SH PMSA 176 83 217.1
SH HOPE 159 78 82.4
SH TRIS 135 79 147.6
SH SACV 86 46 218.1
SH TAM 71 72 169.9
SH BFO 44 70 163.8
−10 0 10 20 30 40
Time (s)
−10 0 10 20 30 40
Time (s)
−10 0 10 20 30 40
Time (s)

DOI: 10.1038/NGEO977

Figure S9

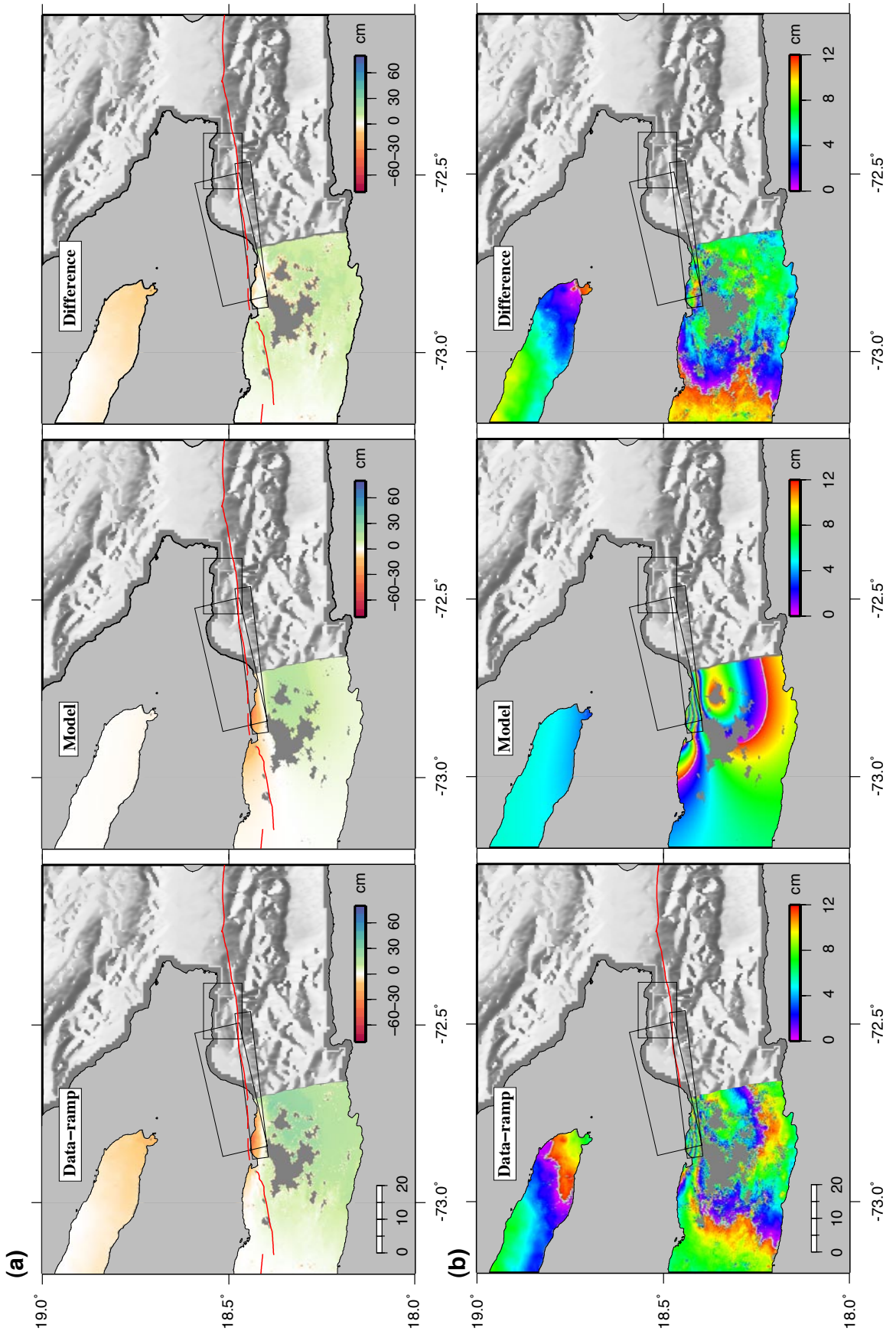

Figure S9

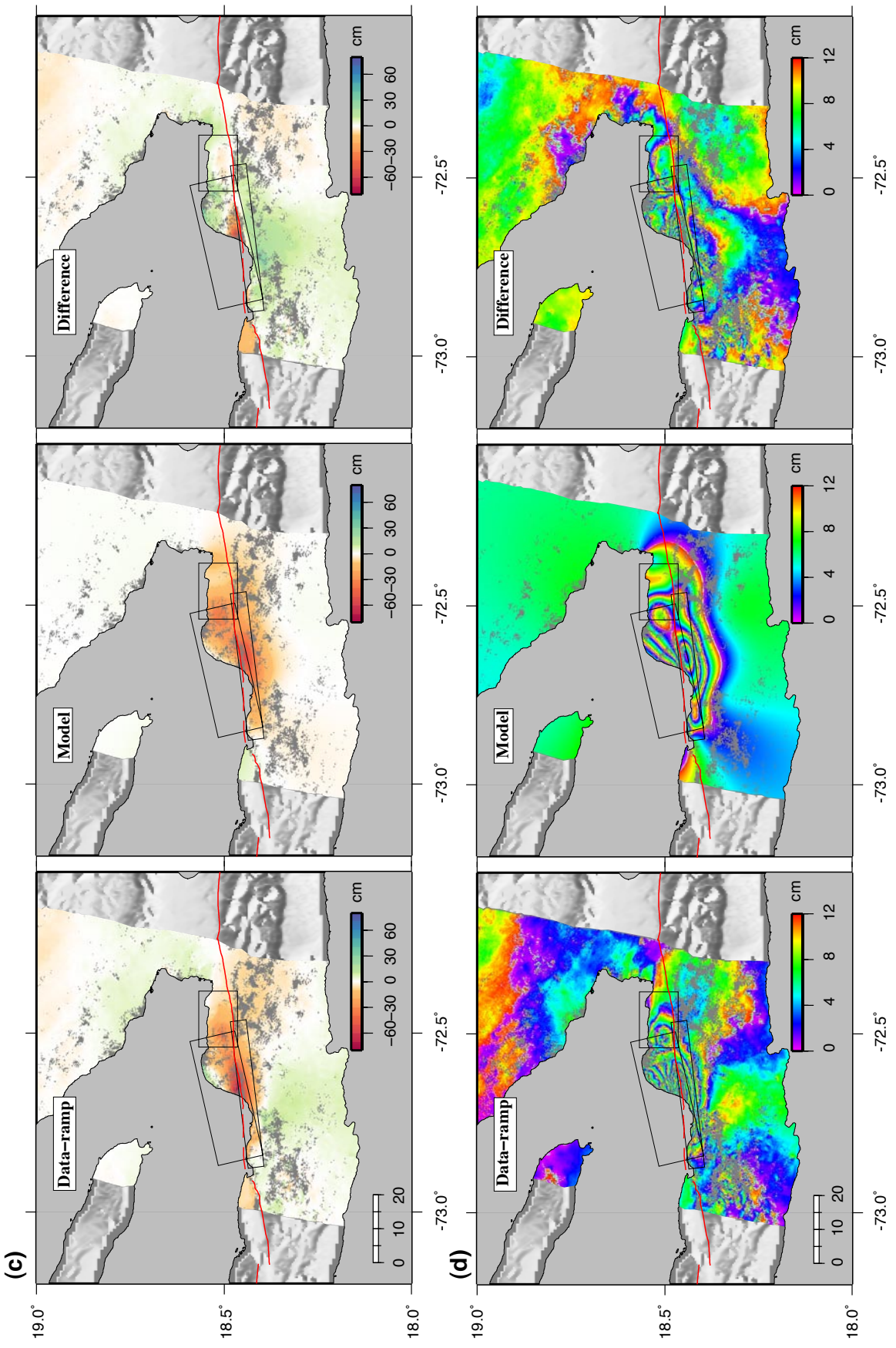
(c)
(d)
Data−ramp
Model
Difference
cm
−60 −30 0 30 60
0 10 20
0 4 8 12
19.0°
18.5°
18.0°
-73.0°
-72.5°

DOI: 10.1038/NGEO977

Figure S9

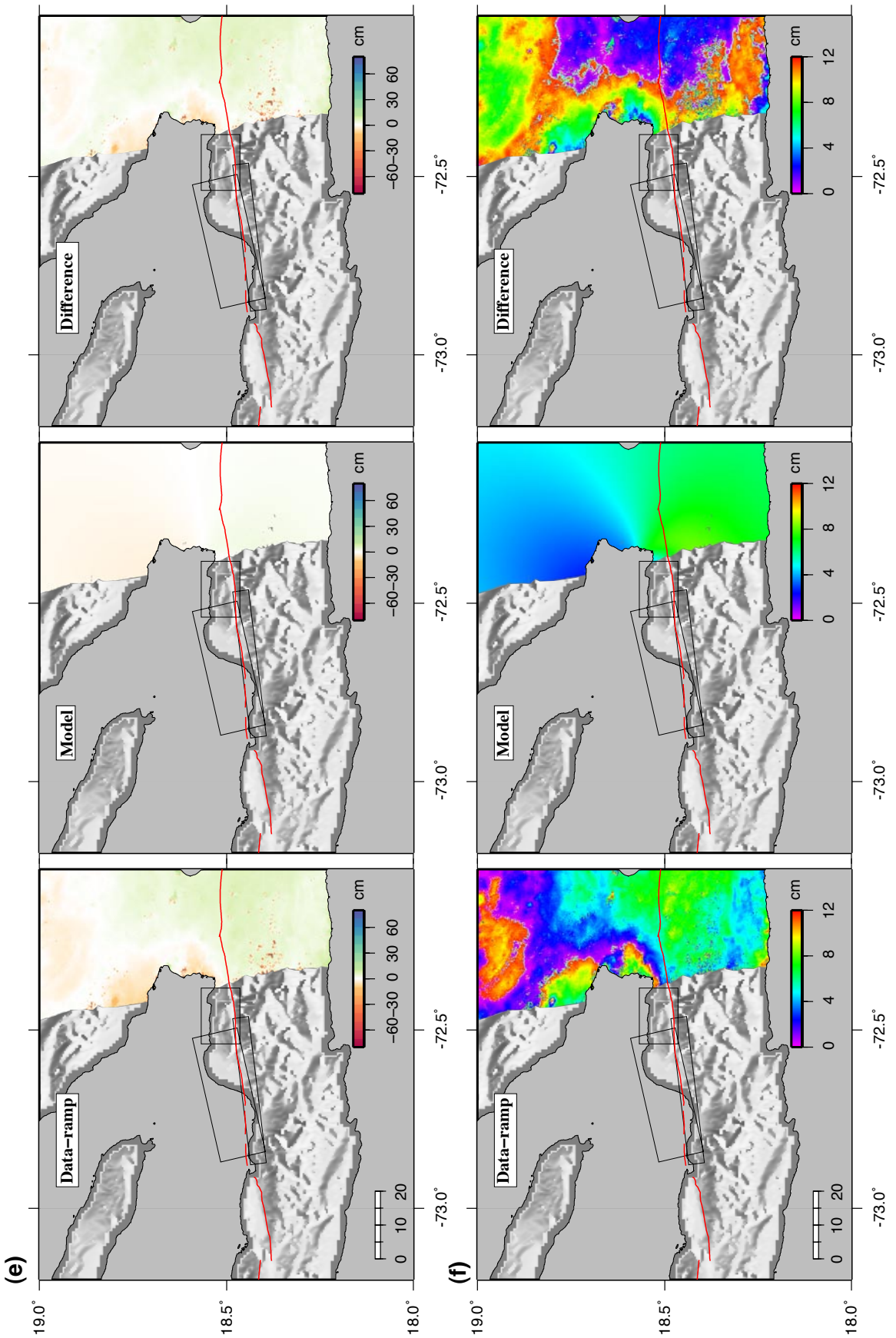

Figure S9

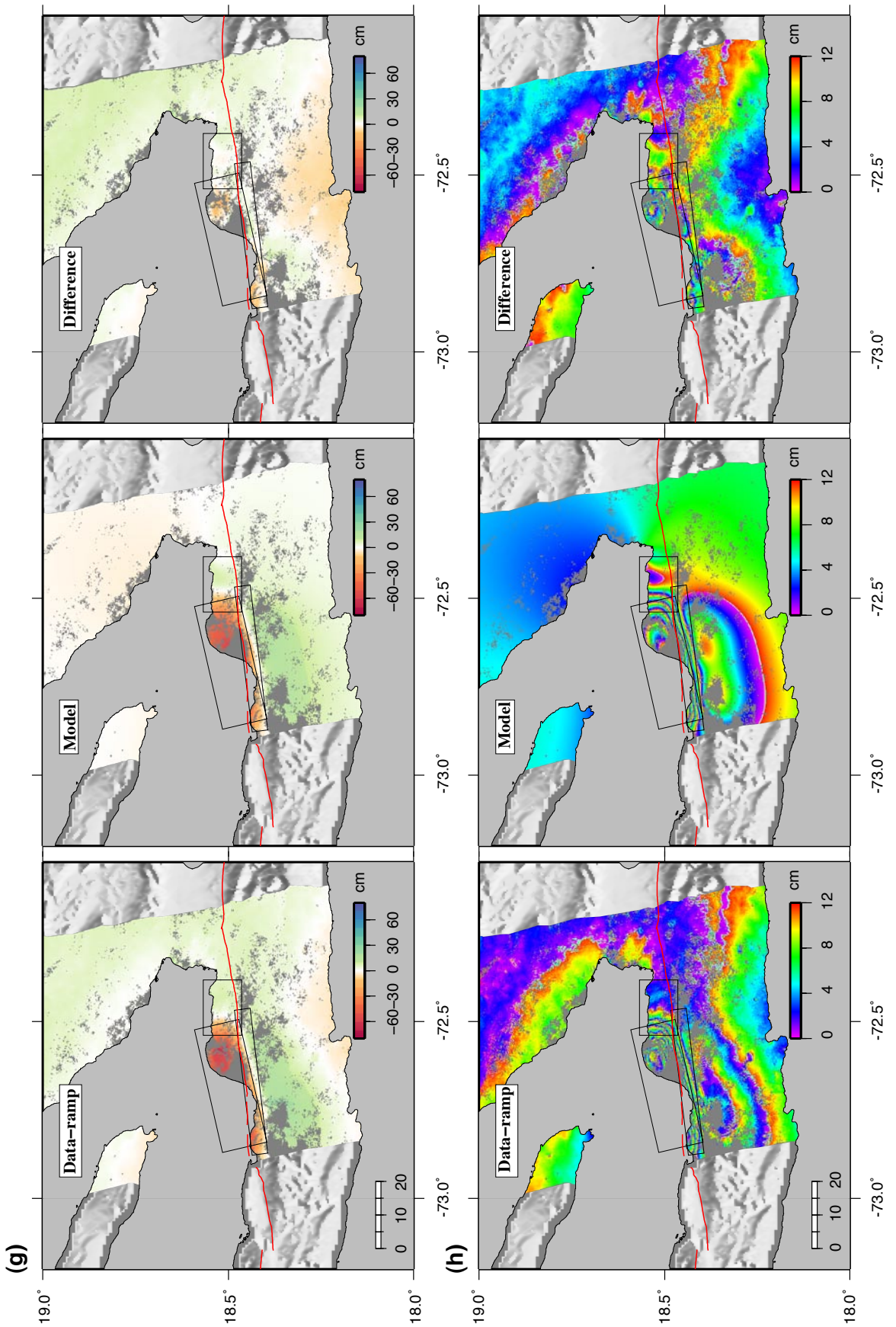
(g)
(h)
Data−ramp
Model
Difference
cm
−60 −30 0 30 60
0 4 8 12
0 10 20
19.0°
18.5°
18.0°
-73.0°
-72.5°

DOI: 10.1038/NGEO977

Figure S10

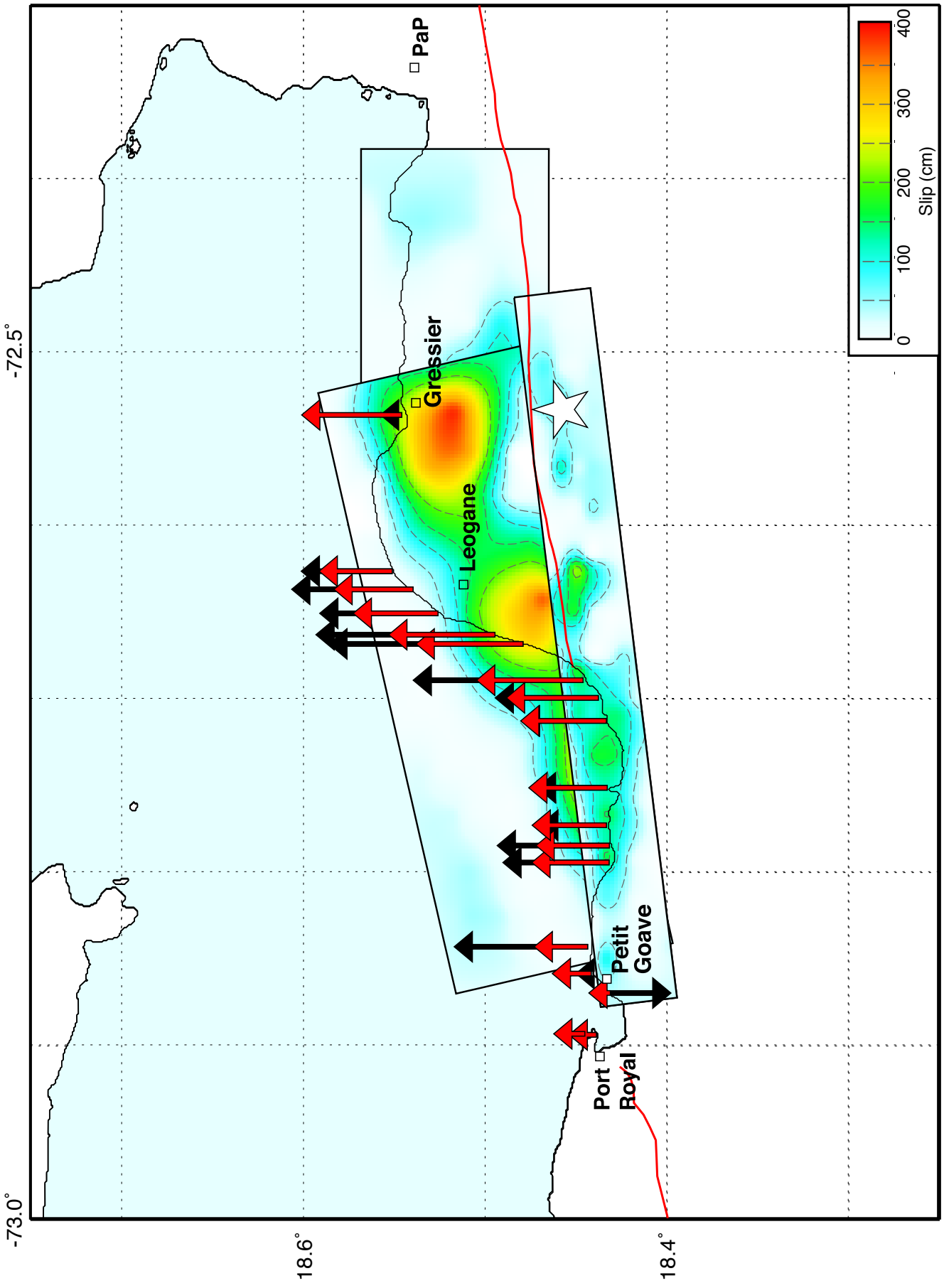

Figure S11

(a)

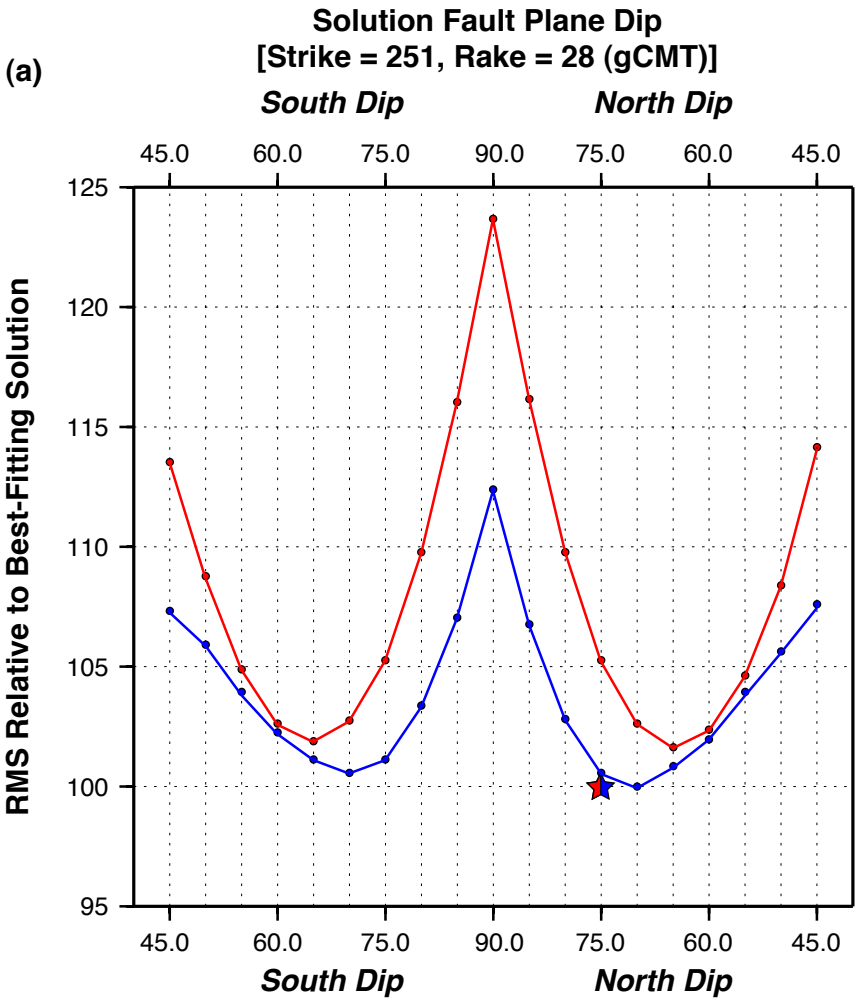

(b)

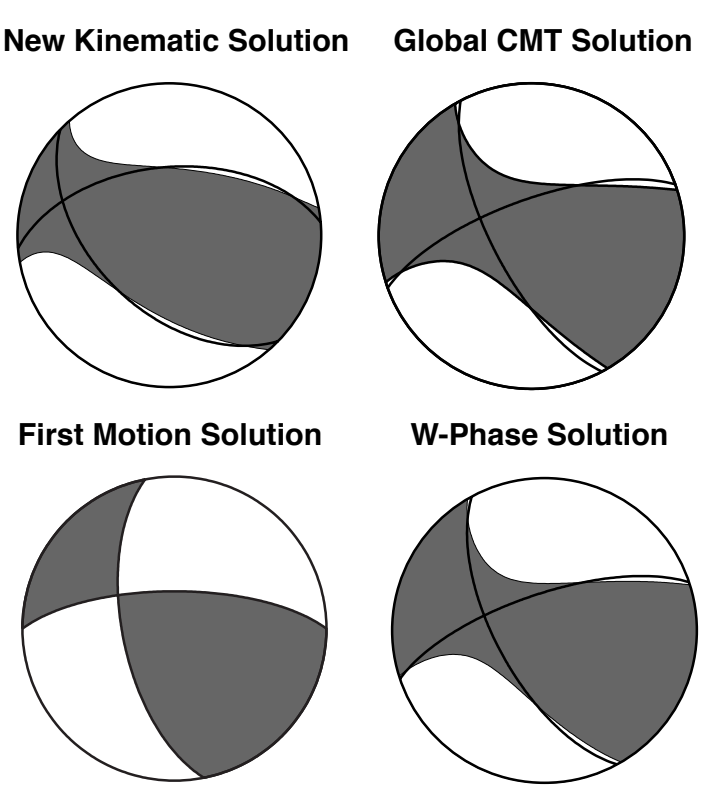

DOI: 10.1038/NGEO977

Figure S12

- Compressional
- Dilatational
- Nodal

First Motions

	Azimuth	Plunge
P-axis	37.9	5.2
T-axis	131.6	35.0
B-axis	300.6	54.5

P1 Strike, Dip, Rake: 270, 70, 30
P2 Strike, Dip, Rake: 169, 62, 157

gCMT

	Azimuth	Plunge
P-axis	19.7	4.0
T-axis	112.4	33.6
B-axis	283.8	56.1

P1 Strike, Dip, Rake: 251, 70, 28
P2 Strike, Dip, Rake: 151, 64, 158

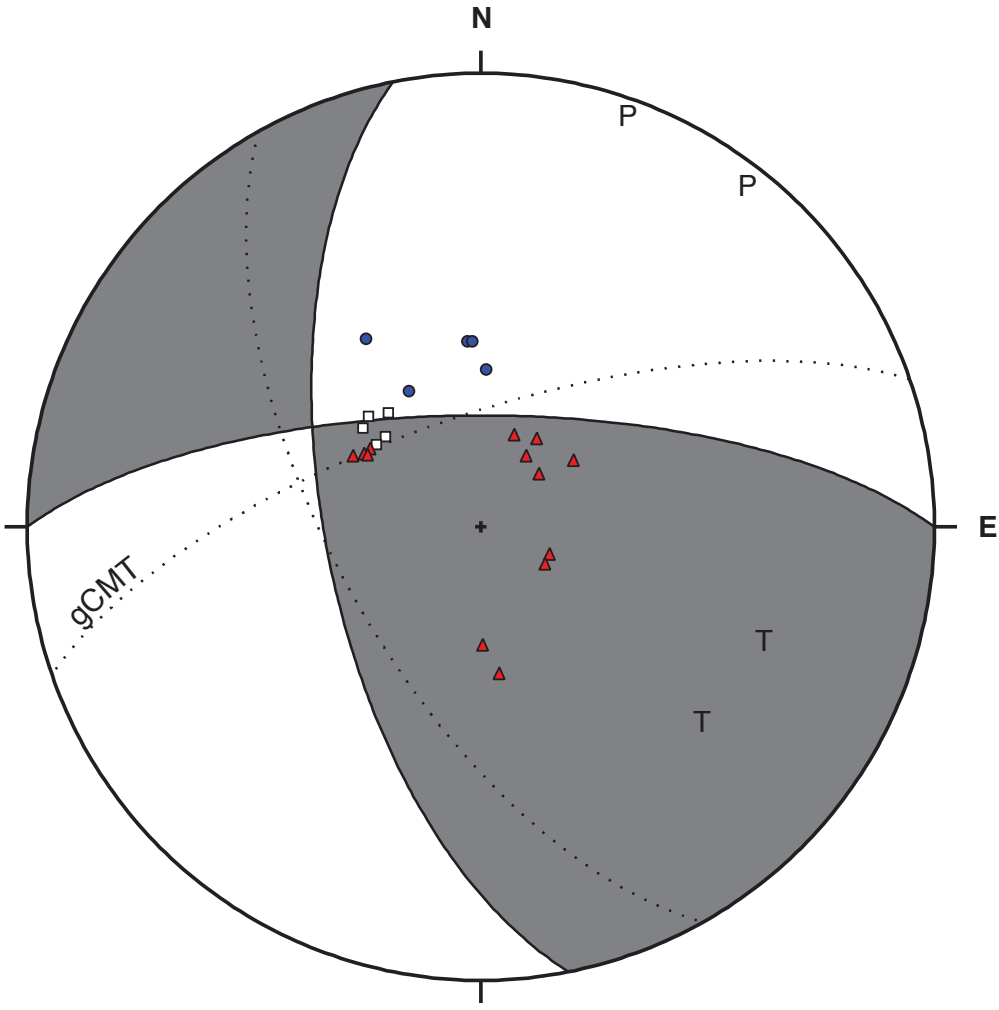

DOI: 10.1038/NGEO977

Table S2. Coastal uplift values determined from coral microatoll and beach geomorphic measurements

Site	Lat.	Lon.	Date (UTC)	Time (UTC)	Tidal stage (m)[1]	Corr. to ELT (m)[2]	App. uplift (m)[3]	Survival correction (m)[4]	UPLIFT (m)[5]	Error (+/-)[6]	Millepora diedown[7]	HLS to HLS[8]	Comments
Beloc	18.479070°	-72.668659°	02.25.2010	16:08:00	0.13	0.31	0.7	0.06	**0.64**	0.11	n/r	0.45 (*Sid.*)	Abundant *Sid. siderea* microatolls
Cassagne (Baussin)	18.494491°	-72.663347°	02.25.2010	18:30:00	0.18	0.36	0.59	n/a	**0.59**	0.18	n/o	n/a	*Sid. siderea* w/o clear HLS; min. uplift
Leogane	18.525851°	-72.651021°	02.25.2010	20:02:00	0.26	0.44	0.45	0.06	**0.39**	0.11	n/o	0.18 (*Sid.*)	Only surviving pre-EQ *Sid. siderea* microatoll in place at Leogane
Kay Mirak	18.539581°	-72.637173°	02.25.2010	21:00:00	0.29	0.47	0.4	n/a	**0.40**	0.12	n/a	n/a	Beach geomorph
Kay Tiyout	18.551034°	-72.626712°	02.25.2010	21:30:00	0.29	0.47	0.3	n/a	**0.30**	0.09	n/a	n/a	Beach geomorph
Tapion de Petit Anglais	18.431660°	-72.794754°	02.26.2010	14:55:00	0.22	0.4	0.35	n/a	**0.35**	0.11	n/a	n/a	Beach geomorph
Port Royal island	18.438644°	-72.894166°	02.26.2010	19:36:00	0.19	0.37	0.15	0.06	**0.09**	0.09	n/o	n/a	No sign of reef die-down; stable or only slightly up
Boyer Island	18.432698°	-72.751661°	02.27.2010	14:39:00	0.21	0.39	0.25	0.02	**0.23**	0.11	0.12	n/a	No *Sid.*; from *Porites* HLS
One Horse Terrace	18.431487°	-72.785005°	02.27.2010	17:30:00	0.08	0.26	0.43	0.06	**0.37**	0.11	0.17	0.14 (*Sid.*)	From *Sid. radians* HLS; value from *Diploria* is 4 cm higher
La Hatte	18.443492°	-72.843347°	02.27.2010	19:18:00	0.1	0.28	0.5	0.06	**0.44**	0.11	0.14	0.22 (*Sid.*)	*Sid. siderea* microatolls
L'acul	18.445996°	-72.689605°	02.27.2010	21:03:00	0.24	0.42	0.62	0.06	**0.56**	0.11	0.1	0.21 (*Sid.*)	*Sid. siderea* microatolls
Fauche	18.433165°	-72.713084°	02.28.2010	15:24:00	0.28	0.46	0.36	0.08	**0.28**	0.11	0.15	0.15 (*Dip.*)	*Diploria* microatolls
Bellevue	18.437596°	-72.699797°	02.28.2010	16:47:00	0.14	0.32	0.42	0.08	**0.34**	0.11	0.19	0.15 (*Dip.*)	*Diploria* microatolls
Grand Goave seawall	18.433123°	-72.773273°	02.28.2010	18:31:00	0.03	0.21	0.3	0.08	**0.22**	0.11	0.16	n/a	*Diploria* microatolls
La Hatte seawall	18.441517°	-72.858818°	03.02.2010	15:16:00	0.36	0.54	0.11	0.06	**0.05**	0.05	n/o	n/o	Reef healthy; no die-down
Port Royal point	18.444990°	-72.893583°	03.02.2010	20:47:00	-0.03	0.15	-0.15	0.06	**-0.21**	0.11	n/o	n/o	Reef healthy; no die-down. Apparent subsidence may be due to normal displacement across Port Royal fracture feature.
Petit Goave pier	18.430988°	-72.870051°	03.02.2010	15:45:00	0.32	0.5	-0.15	n/a	**-0.15**	0.15	n/a	n/a	Estimate from undeformed pier, standing water, and eyewitness accounts
Passion Beach	18.545808°	-72.536580°	03.03.2010	17:00:00	0.24	0.42	0.07	n/a	**0.07**	0.07	0.07	.03 (*P. ast.*)	*Sid. siderea* shows zero uplift, but average 7 cm die-down of *Millepora*, some stressed sea grass.
Ile de la Gonave	18.699632°	-72.813333°	03.04.2010	15:38:00	0.31	0.49	0	0	**0.00**	0.11	n/o	n/a	This reference site is used to evaluate HLS wrt ELT and thus uplift is defined as zero

[1] Tidal stage at time of measurement is arbitrary. Tide model is derived from prediction at Port-au-Prince adjusted to fit Ile de la Gonave temporary deployment (Roger Bilham, personal communication)
[2] Absolute correction to reach Extreme Low Tide (ELT) as predicted from interval 2000 - 2010 (-0.18 m in this arbitrary datum).
[3] Apparent uplift is with respect to water level at time of observation and not corrected for future die-down
[4] Survival correction for expected coral survival above ELT as calibrated by Ile de la Gonave observations (2 cm for *Porites*, 6 cm for *Siderastrea*, 8 cm for *Diploria*)
[5] Uplift is vertical displacement with respect to pre-earthquake elevation
[6] For coral measurements, error is calculated as root of the sum of the squares of instrument error (1 cm), tide model error (5 cm), and sea level anomaly uncertainty (10 cm).
For non-coral measurements, uncertainty is assumed to be 30% of measured value.
[7] Diedown of *Millepora complanata* corals is a minimum measure of uplift. n/r = not recorded, n/o = not observed
[8] Differences in pre- and post-EQ HLS (Highest Level of Survival) are a minimum estimate of uplift; further die-downs are predicted. *Sid. = Siderea siderastrea, Dip. = Diploria strigosa, P. ast. = Porites asteroides*

DOI: 10.1038/NGEO977

Table S3. Qualitative indicators of vertical motion

Site	Lat	Long	Date	Description	Qualitative assessment of vertical motion
1	18.4307019	-72.71918605	24-FEB-10 3:16:06PM	Reef shallow, beach widened	up
2	18.4317162	-72.71681271	24-FEB-10 3:18:31PM	Reef shallow, beach widened	up
3	18.4333789	-72.71688446	24-FEB-10 3:24:34PM	Millepora exposed	up
4	18.434604	-72.71355266	24-FEB-10 3:29:36PM	Reef exposed, beach widened	up
5	18.4355972	-72.71106675	24-FEB-10 3:32:56PM	Coral exposed and dying	up
6	18.437789	-72.6981727	24-FEB-10 3:43:04PM	Secondary failure of delta front	2nd down
7	18.4374697	-72.69686094	24-FEB-10 3:53:08PM	Reef exposed at Beloc site	up
8	18.4945245	-72.66335771	25-FEB-10 12:44:29PM	Small exposed patch reef at Cassagne (Baussin) site	up
9	18.5258676	-72.65101385	25-FEB-10 2:06:28PM	Exposed reef at Leogane microatoll site	up
10	18.5395808	-72.63717332	25-FEB-10 3:01:22PM	Widened beach face at Kay Mirak site	up
11	18.5510345	-72.62671195	25-FEB-10 3:35:36PM	Widened beach face at Kay Tiyout site	up
12	18.4316604	-72.79475385	26-FEB-10 9:14:50AM	Widened beach face, exposed boulders at Tapion de Petit Anglais site	up
13	18.4394314	-72.80415365	26-FEB-10 9:25:49AM	Double notch in boulder - sequential uplift	up
14	18.4437524	-72.83337054	26-FEB-10 9:39:52AM	Clear coastal emergence from here to west	up
15	18.4389291	-72.8624394	26-FEB-10 9:56:03AM	Stranded stairs indicate uplift	up
16	18.4300102	-72.87143754	26-FEB-10 10:09:07AM	Pier stable or down; then down to west	down
17	18.4252956	-72.88012362	26-FEB-10 10:16:38AM	Minor subsidence, not clearly secondary	down
18	18.4256964	-72.8866553	26-FEB-10 10:19:14AM	Severe slumping delta front	2nd down
19	18.4282844	-72.89536167	26-FEB-10 10:23:01AM	Still subs from prev. point; veg drowned; storm berm breached	down
20	18.4345478	-72.89798269	26-FEB-10 10:25:47AM	Still subs from prev. point; veg drowned; storm berm breached	down
21	18.4387266	-72.89876162	26-FEB-10 10:28:14AM	Drowned vegetation (clearly secondary on imagery)	2nd down
22	18.4460768	-72.89418644	26-FEB-10 11:34:06AM	Healthy reef, no obvious uplift	0
23	18.4459045	-72.89414755	26-FEB-10 11:51:25AM	Notch in reef suggests no sig. uplift	0
24	18.4381306	-72.89951683	26-FEB-10 12:43:02PM	Drowned veg (clearly secondary on imagery)	2nd down
25	18.4390874	-72.89594161	26-FEB-10 3:17:10PM	No clear change at Port Royal Island site	0
26	18.4329545	-72.75116058	27-FEB-10 9:04:10AM	Exposed reef at Boyer Island site	up
27	18.4314869	-72.78500469	27-FEB-10 10:18:28AM	Exposed reef at One Horse Terrace site	up
28	18.4434922	-72.84334701	27-FEB-10 1:22:21PM	Exposed reef at La Hatte site	up
29	18.4331645	-72.71308394	28-FEB-10 9:40:12AM	Exposed reef at Fauche site	up
30	18.4375957	-72.69979653	28-FEB-10 11:21:14AM	Exposed reef at Bellevue site	up
31	18.4331229	-72.77327296	28-FEB-10 1:18:10PM	Exposed reef at Grand Goave seawall site	up
32	18.4413898	-72.85838641	02-MAR-10 9:44:13AM	Reef not stressed at La Hatte seawall site; beach slightly widened	up
33	18.4397028	-72.86119904	02-MAR-10 10:31:54AM	Stairs stranded	up
34	18.4387702	-72.86210806	02-MAR-10 10:32:43AM	Stairs stranded	
35	18.4376805	-72.86371579	02-MAR-10 10:33:54AM	Apparently stable	0
36	18.4364551	-72.86592007	02-MAR-10 10:35:28AM	Canal seems stable	0
37	18.4348208	-72.86734449	02-MAR-10 10:37:44AM	Berm forming on landward terrace	down
38	18.4343465	-72.86846808	02-MAR-10 10:38:54AM	Canal mouth flooded	down
39	18.4343554	-72.86797833	02-MAR-10 10:41:22AM	Accelerated cliff retreat	down
40	18.4286098	-72.86775076	02-MAR-10 11:02:54AM	To here from pier no prom. secondary deformation	0
41	18.4282031	-72.86874468	02-MAR-10 11:07:51AM	Canal wall is stable, not displaced	0
42	18.4298827	-72.87107351	02-MAR-10 11:30:25AM	Begin drowned trees to W	2nd down
43	18.429464	-72.87146646	02-MAR-10 11:31:08AM	Drowned palms	2nd down
44	18.4264393	-72.87405152	02-MAR-10 11:36:30AM	Base of structure inund. at 11:35 am local time	2nd down
45	18.4257852	-72.87450565	02-MAR-10 11:38:22AM	Building flooded 20 cm at 11:38 am local time	2nd down
46	18.4253564	-72.87548164	02-MAR-10 11:56:58AM	Canal deformed by shaking, back-rotated	2nd down
47	18.4246776	-72.87793091	02-MAR-10 12:00:09PM	No obvious secondary deformation but drowned vegetation	down
48	18.4247059	-72.87896289	02-MAR-10 12:01:32PM	Canal flooded, only minor secondary def	2nd down
49	18.4249045	-72.88020082	02-MAR-10 12:03:12PM	Palms appear in normal position wrt tide	0
50	18.4252482	-72.88198038	02-MAR-10 12:05:39PM	Normal looking palms	0
51	18.4255881	-72.88687818	02-MAR-10 12:12:23PM	To here from previous, normal or <20-30 cm subs	0
52	18.4271556	-72.89423229	02-MAR-10 12:17:52PM	Coast appears normal	0
53	18.4296255	-72.8962214	02-MAR-10 12:20:08PM	Coast appears normal	0
54	18.4318622	-72.89769779	02-MAR-10 12:22:06PM	Beach face appears slightly widened	up
55	18.4351176	-72.89909539	02-MAR-10 12:36:15PM	Oficier: Locals say up 20 cm	up
56	18.4406925	-72.89229641	02-MAR-10 1:06:07PM	Mangroves not distressed - no apparent change	0
57	18.4430648	-72.89244728	02-MAR-10 1:18:16PM	Stable or slightly up - no clear change	0
58	18.4431674	-72.89338698	02-MAR-10 1:32:52PM	Slightly up? Dead *Thalassia*	0
59	18.4484779	-72.89493126	02-MAR-10 4:23:37PM	Coast normal	0
60	18.5447588	-72.53769471	03-MAR-10 10:53:38AM	Stressed reef at Passion Beach	up
61	18.5635406	-72.59934529	03-MAR-10 12:54:38PM	Coast up, secondary deformation imprint	up
62	18.6934526	-72.82142314	04-MAR-10 9:30:36AM	Gonave - stable with deep notch	0
63	18.4460811	-72.68968293	04-MAR-10 3:10:37PM	Exposed reef at L'acul site	up